Chemical Science

Accepted Manuscript

This article can be cited before page numbers have been issued, to do this please use: Z. Zheng, Q. Chen, P. Su, L. Cai, J. Liang, G. Xiao and F. Xiao, *Chem. Sci.*, 2026, DOI: 10.1039/D6SC02262F.

ROYAL SOCIETY OF CHEMISTRY

rsc.li/chemical-science

Cascade Charge-Transport-Chain Engineering in Alloy Nanocluster-Semiconductor Artificial Photosystems

View Article Online
DOI: 10.1039/D6SC02262F

Zi-Han Zheng[a], Qing Chen[a], Peng Su[a], Lifeng Cai*[b], Jie Liang[b], Guangcan Xiao[c], Fang-Xing Xiao*[a]

a. College of Materials Science and Engineering, Fuzhou University, New Campus, Fujian Province, 350116, P. R. China.

b. College of Environmental and Biological Engineering, Fujian Provincial Key Laboratory of Ecology-Toxicological Effects & Control for Emerging Contaminants, Putian University, Putian, Fujian, 351100, P. R. China.

c. Instrumental Measurement and Analysis Center, Fuzhou University, Fuzhou 350108, P.R. China.

E-mail: 89437499@qq.com; fxxiao@fzu.edu.cn

Abstract

Atomically precise metal nanoclusters (NCs), featuring discrete electronic structure and pronounced quantum confinement effects, are emerging as promising photosensitizers for artificial photosystems; however, their practical implementation remains fundamentally constrained by rapid charge recombination and poorly controlled charge transport. Here, we introduce a conceptual cascade charge-transport-chain engineering strategy that addresses this intrinsic bottleneck by constructing directional and continuous carrier transport pathways across NC-semiconductor interfaces. By integrating alloy NCs photosensitization with atomic Ni doping of TiO_2, a robust interfacial electronic coupling is established, enabling directional and accelerated extraction of photogenerated carriers. The resulting BNC/Ni-TiO_2 heterostructures exhibit markedly enhanced visible-light-driven hydrogen evolution, accompanied by effective suppression of charge recombination within alloy NCs. Combined experimental and theoretical investigations reveal that the performance

enhancement originates from cascade charge-transport-chain engineering rather than simple binary synergy. This work provides a general design principle for constructing tunable charge-transport pathways with alloy NCs, advancing NC-based artificial photosystems toward solar-to-hydrogen energy conversion.

View Article Online
DOI: 10.1039/D6SC02262F

Keywords: Bimetallic nanoclusters, Ni doping, Photocatalytic hydrogen generation, Charge transfer, Titanium dioxide.

1. Introduction

Atomically precise nanoclusters (NCs) with discrete electronic structures and pronounced quantum confinement effects, have emerged as promising photosensitizers for artificial photosystems, owing to their superior light-harvesting properties.[1,2] However, the widespread application of metal NCs is hindered by fundamental challenges, such as rapid charge recombination and poorly controlled charge transport, which prevent the construction of stable and efficient metal NCs-based systems.[3]

In recent years, heterometallic NCs particularly bimetallic NCs (BNCs) have garnered increasing attention as a new generation of light-harvesting antennae for solar energy conversion. BNCs are synthesized by incorporating two different metals into a single nanocluster unit, offer a promising strategy to overcome the inherent limitations of traditional monometallic NCs through bimetallic synergy. Through atomic-scale manipulation of metal composition and spatial arrangement, BNCs offer distinct advantages, including: (i) precise control of their geometric and electronic structures; (ii) enhanced light-harvesting efficiency, and (iii) accelerated charge transport kinetics. These features position BNCs as ideal active centers for photon capture and catalytic reactions.[4] Despite these compelling merits, the use of BNCs as photocatalysts remains limited by poor charge separation efficiency and low photocatalytic activity. To address these challenges, one promising strategy is the coupling of BNCs with metal oxide semiconductors, such as titanium dioxide (TiO_2), to form heterostructures with optimized energy level alignment. This integration extends the photo-response range of metal oxide substrate and enhances charge migration and separation over the BNCs, facilitating efficient photoredox catalysis. However, achieving efficient charge transport and separation remains a critical issue in the design of high-performance artificial photosystems.

View Article Online
DOI: 10.1039/D6SC02262F

A promising solution lies in the deposition of suitable co-catalysts (e.g., Ru, Pd, Pt) on TiO_2 surface, which increases the number of active sites for accelerated photocatalytic reactions while mitigating carrier recombination.[5] Among these co-catalysts, nickel (Ni) stands out as a low-cost and efficient option for photocatalytic hydrogen generation due to its ability to boost charge transfer kinetics and its strong affinity for active hydrogen species.[6] Combining Ni with BNCs offers a dual-functional strategy for increasing the number of active sites on TiO_2 and extending the visible light absorption capabilities of TiO_2, which together maximizes solar energy utilization and drives charge flow.[6b, 7] By strategically incorporating Ni co-catalysts and simultaneously anchoring alloy NCs ($Au_{1-x}Ag_x$, $Au_{1-x}Pt_x$, $Au_{1-x}Cu_x$) onto TiO_2, and fine-tuning of interface configuration, we hypothesize that controllable charge transport pathway can be stimulated. Once the applicable energy level alignment between the components is optimized, this will facilitate accelerated directional charge migration and suppress carrier recombination, ultimately leading to the significantly improved photocatalytic hydrogen production performance under visible light. This integrated strategy paves the way for the development of novel alloy NCs-based artificial photosystems.

Inspired by these insights, herein, we conceptually present a cascade charge-transport-chain engineering strategy via constructing TiO_2-Ni/BNCs ($Au_{1-x}Ag_x$, $Au_{1-x}Pt_x$, $Au_{1-x}Cu_x$) heterostructure artificial photosystems for solar-to-hydrogen conversion. Specifically, Ni is doped onto the surface of TiO_2 nanosheets via a molten-salt method (MSM), followed by electrostatic self-assembly of tailor-made alloy NCs onto the Ni-doped TiO_2 (TiO_2-Ni) to form the TiO_2-Ni/BNCs ($Au_{1-x}Ag_x$, $Au_{1-x}Pt_x$, $Au_{1-x}Cu_x$) ternary photocatalysts. The results demonstrate that the photosensitization effect of BNCs broadens the light absorption range of pristine TiO_2, while the accelerated interfacial charge transfer enabled by Ni doping significantly enhances the photocatalytic hydrogen evolution activities of the TiO_2-Ni/BNCs heterostructures under visible light. Through a combination of experimental and theoretical investigations, we elucidate the charge transfer mechanism within the TiO_2-Ni/BNCs photosystems, revealing a synergistic effect between atomic-scale BNCs and metal oxide supports. This work highlights the promising potential of BNCs as high-performance photosensitizers and presents a novel approach to engineering cascade charge-transport-chains that enhance the efficiency of metal NCs-semiconductor hybrid artificial photosystems for efficient solar-to-hydrogen energy conversion.

2. Experimental section

2.1 Materials

All the materials were of analytical grade and used as received without further purification, and the detailed information was provided in *Supporting Information (SI)*.

View Article Online
DOI: 10.1039/D6SC02262F

2.2 Preparation of photocatalysts

2.2.1 Preparation of TiO_2 nanosheets

Under vigorous stirring, 4.9 mL 40 wt% hydrofluoric acid (HF) solution was dropped into 50 mL of tetrabutyl titanate (TBOT) in a 100 mL Teflon bottle sealed with a stainless steel autoclave. The mixture was heated in an electric oven at 180 °C for 24 h to get a white powder. The separated solid was successively washed with ethanol, 0.1 M NaOH, and deionized water, respectively, to obtain the TiO_2 nanosheets.[8]

2.2.2 Preparation of TiO_2-Ni nanocomposites

TiO_2-Ni is prepared by a modified molten-salt method. In a typical process, 10 mg of $NiCl_2 \cdot 6H_2O$, 0.9 g of LiCl, 1.1 g of KCl and 1 g of TiO_2 nanosheets are pestled in a mortar for 0.5 h to make a uniform mixture, which is then transferred into a semi-capped corundum crucible. Next, the crucible is put into a tube furnace and calcined at 773 K for 2 h under N_2 atmosphere (heating rate: 8 K/min). After cooling down to 298 K naturally, the mixture is washed with deionized water thoroughly for five times to remove the salt (LiCl & KCl) and then thus-obtained TiO_2-$Ni_{0.25}$ was dried in a vacuum oven at 333 K.[9] In addition, the loading amount of Ni is tuned by adding 5, 10, 20, 40 mg of $NiCl_2 \cdot 6H_2O$ in the receipt, and the mixture were labeled as TiO_2-Ni_m (m = 0.12, 0.25, 0.46, 0.93).

2.2.3 Preparation of bimetallic NCs

$Au_{1-x}Ag_x$ NCs were synthesized according to a previous work with some modifications.[10] Aqueous solutions of $HAuCl_4$ (20 mM, 0.50 mL), $AgNO_3$ (20 mM, 0.10 mL) and GSH (100 mM, 0.15 mL) were mixed with 4.35 mL of deionized water at 25 °C. The reaction mixture was heated to 70 °C under gentle stirring (1000 rpm) for 24 h in air. Then $Au_{1-x}Ag_x$ NCs were cool down to room temperature to obtain a yellow solution, which was stored in a refrigerator at 4 °C for further use. The fabrication of $Au_{1-x}Cu_x$ NCs and $Au_{1-x}Pt_x$ NCs is akin to that of the $Au_{1-x}Ag_x$ NCs by replacing $AgNO_3$ with $Cu(NO_3)_2$ and chloroplatinic acid hexahydrate ($H_2PtCl_6 \cdot 6H_2O$), respectively.

2.2.4 Preparation of TiO_2-Ni/BNCs heterostructures

0.1 g TiO_2-Ni_m was dispersed into $Au_{1-x}Ag_x$ NCs aqueous solution at under vigorous stirring (1000 rpm) for 1 h. Pre-set X mL (X= 5, 7, 10, 13, 15) of $Au_{1-x}Ag_x$ NCs aqueous solution was diluted to different concentration with deionized water. The reaction mixture was centrifuged, then washed with ethanol, deionized water and dried in vacuum at 60 ℃ for 8 h. The mixtures were labeled as TiO_2-Ni_m/n$Au_{1-x}Ag_x$ (n = 5, 7, 10, 13, 15). When the photocatalyst contains 0.25 wt% of Ni and 10 mL of $Au_{1-x}Ag_x$ NCs, which represents the optimal sample for the subsequent systematic investigation and is defined as T-$Ni_{0.25}$/$Au_{1-x}Ag_x$. Similarly, the preparation of TiO_2-$Ni_{0.25}$/$Au_{1-x}Cu_x$ and TiO_2-$Ni_{0.25}$/$Au_{1-x}Pt_x$ followed the same procedure as that for T-$Ni_{0.25}$/$Au_{1-x}Ag_x$, using 10 mL of $Au_{1-x}Cu_x$ and $Au_{1-x}Pt_x$ precursor solutions, respectively, in place of $Au_{1-x}Ag_x$.

2.3 Characterization

The crystal structure was determined by X-ray diffraction (XRD, Miniflex600). Morphologies were visualized by field emission scanning electron microscopy (FESEM, Supra55, Carl Zeiss) equipped with energy-dispersive spectroscopy (EDS) and transmission electron microscopy (TEM, Tecnai G2 F20). Fourier transform infrared (FTIR) spectra were recorded on an infrared spectrophotometer (TJ270-30A). Raman spectra were collected with a Raman spectrometer (Dxr-2xi, Thermo Scientific, America). UV-visible diffuse reflectance spectra (DRS) were measured on Cary50 (Varian, America) with the reflectance background from 200 to 800 nm. X-ray photoelectron spectra (XPS) were recorded on a photoelectron spectrometer (ESCALAB 250, Thermo Scientific, America), and the binding energy (BE) of the elements were calibrated by the BE of C 1s (284.80 eV). Zeta potential (ξ) measurements were performed by dynamic light scattering analysis (Zeta sizer Nano ZS-90). Time-resolved photoluminescence (TRPL) spectra were measured on a FLS 920 florescence lifetime spectrophotometer (Edinburgh, Instruments, UK). The photoluminescence (PL) spectra were probed on a Varian Cary Eclipse spectrophotometer. Brunauer-Emmett-Teller (BET) specific surface area and N_2 adsorption experiments were performed on ASAP 2460. Concentrations of T-$N_{0.25}$/10$Au_{1-x}Ag_x$ is quantified by inductively coupled plasma emission spectroscopy (ICP, XSERIES 2 ICP-MS). X-ray absorption fine structure (XAFS) spectroscopy was carried out using the Rapid XAFS 2M (Anhui Absorption Spectroscopy Analysis Instrument Co., Ltd.) by transmission (or Fluorescence) mode at 20 kV and 30 mA. Kelvin-Probe Force Microscopy (KPFM) was performed on Dimension Icon (Bruker, America).

2.4 Photocatalytic H_2 production performances

View Article Online
DOI: 10.1039/D6SC02262F

Photocatalytic reactions were conducted on an online photocatalytic hydrogen production system using a Pyrex vessel. Specifically, 10 mg of the catalyst was dispersed in mixed solution (DI H_2O, 2 mL), then triethanolamine (TEOA, 0.5 mL) was added as the sacrificial agent. The photocatalytic system was thoroughly degassed and irradiated by a 300 W Xe lamp (PLS-SXE300D, Beijing Perfectlight Technology Co., Ltd.) equipped with a 420 nm-cut-off optical filter ($\lambda > 420$ nm). A continuous magnetic stirrer was applied at the bottom of the reactor to keep the catalyst in a suspension status during the whole experiment. The evolved H_2 was monitored periodically by an online gas chromatograph (Shimadzu GC-8A with an MS-5A column using argon as carrier gas). Photoactivities were evaluated based on the H_2 evolution amount in the first 2 h of the reaction. Cyclic photocatalytic H_2 evolution reactions were carried out as follows. Specifically, the photocatalytic system was thoroughly degassed again after the first run without separating the catalysts and supplementing the TEOA. Subsequently, the thoroughly degassed system was irradiated again by a 300 W Xe lamp S10 with a UV-CUT filter to cut off light with a wavelength $\lambda < 420$ nm. Analogously, the following four runs of photocatalytic recycling tests were performed.

2.5 Photoelectrochemical (PEC) measurements

PEC measurements were carried out on an electrochemical workstation (CHI660E, CHI Shanghai, Inc.) and irradiated with visible light ($\lambda > 420$ nm) (PLS-SXE300D, Beijing Perfect Light Co. Ltd., China), with conventional three-electrode system and 0.5 M Na_2SO_4 aqueous solution (pH = 6.69) was utilized as the electrolyte. The three-electrode system is composed of Pt foil (1 cm × 1 cm) as the counter electrode, Ag/AgCl electrode as the reference electrode and working electrodes. The working electrodes were prepared on fluorine-doped tin oxide (FTO) glass that was cleaned by sonication in DI H_2O and ethanol for 30 min and dried at 60 ℃ in an oven. The specific operational information was provided in the SI.

3. Results and discussion

3.1 Structural characterizations

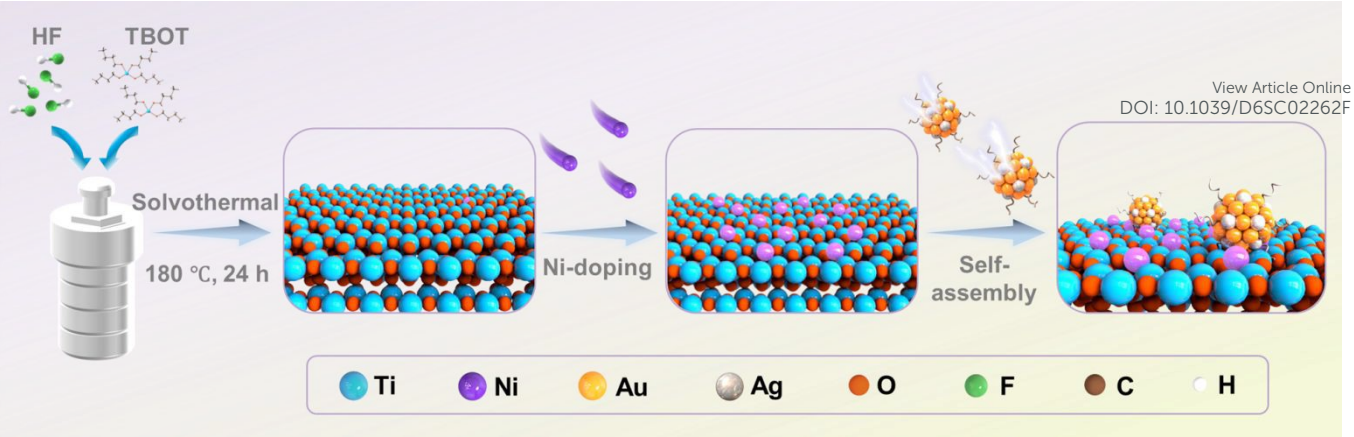

Scheme 1. Schematic flowchart depicting the fabrication of TiO_2-$Ni_{0.25}$/$Au_{1-x}Ag_x$ heterostructures.

The synthesis procedures of TiO_2-$Ni_{0.25}$/$Au_{1-x}Ag_x$ ternary heterostructure are depicted in **Scheme 1**. Initially, the Ni element was doped on the TiO_2 nanosheets by MSM. Upon reaching the melting point of 625 K, the salts form a liquid phase, $NiCl_2$ dissolves and dispersed, generating a strong polarizing force (a pool of ionized anions and cations).[11] This force destabilizes the Ti–O bonds on the surface of TiO_2 nanosheets, facilitating the formation of Ni–O bonds between surface oxygen ions and mobile Ni^{2+} ions. Furthermore, inserting Ni^{2+} ions into the pre-formed, tightly bonded TiO_2 lattice would require overcoming both lattice distortion energy and high diffusion energy barriers, which is thermodynamically unfavorable.[12] Therefore, the MSM promotes the formation of stable Ni–O bonds on the TiO_2 surface at relatively low temperature, thereby effectively preserving the structural integrity of the TiO_2 structures. Subsequently, $Au_{1-x}Ag_x$ NCs were deposited onto the Ni-doped TiO_2 (TiO_2-Ni) through electrostatic self-assembly under ambient conditions, resulting in the TiO_2-Ni/$Au_{1-x}Ag_x$ ternary heterostructures. More specifically, under acidic conditions, abundant hydroxyl (-OH) groups on the surface of TiO_2 facilitate the protons (H^+) migration and adsorption, rendering the positively charged surface.[13] Given the surface of $Au_{1-x}Ag_x$ NCs (ca. 1.7 nm) are capped with glutathione (GSH) ligands bearing carboxyl ($-COO^-$) functional groups, and thus they are featured by negatively charged surface (**Figure S1**). Thus, negatively charged $Au_{1-x}Ag_x$ NCs are attracted by the positively charged TiO_2 substrate via electrostatic interaction, ultimately forming the TiO_2/$Au_{1-x}Ag_x$ NCs heterostructure under ambient conditions. Similarly, Ni-doped TiO_2 assembles with the $Au_{1-x}Ag_x$ NCs in the same way, giving rise to the TiO_2-Ni/$Au_{1-x}Ag_x$ NCs heterostructure. After Ni doping and $Au_{1-x}Ag_x$ NCs decoration, the color of the samples gradually changes from white to yellow (**Figure S2**), indicating the successful modification of TiO_2. This electrostatic self-assembly strategy is also utilized to fabricate the TiO_2-Ni/alloy NCs ($Au_{1-x}Pt_x$, $Au_{1-x}Cu_x$) ternary

heterostructures. The detailed characterizations of $Au_{1-x}Cu_x$ and $Au_{1-x}Pt_x$ NCs are specifically illustrated in **Figure S3** and **Figure S4**, respectively.

View Article Online
DOI: 10.1039/D6SC02262F

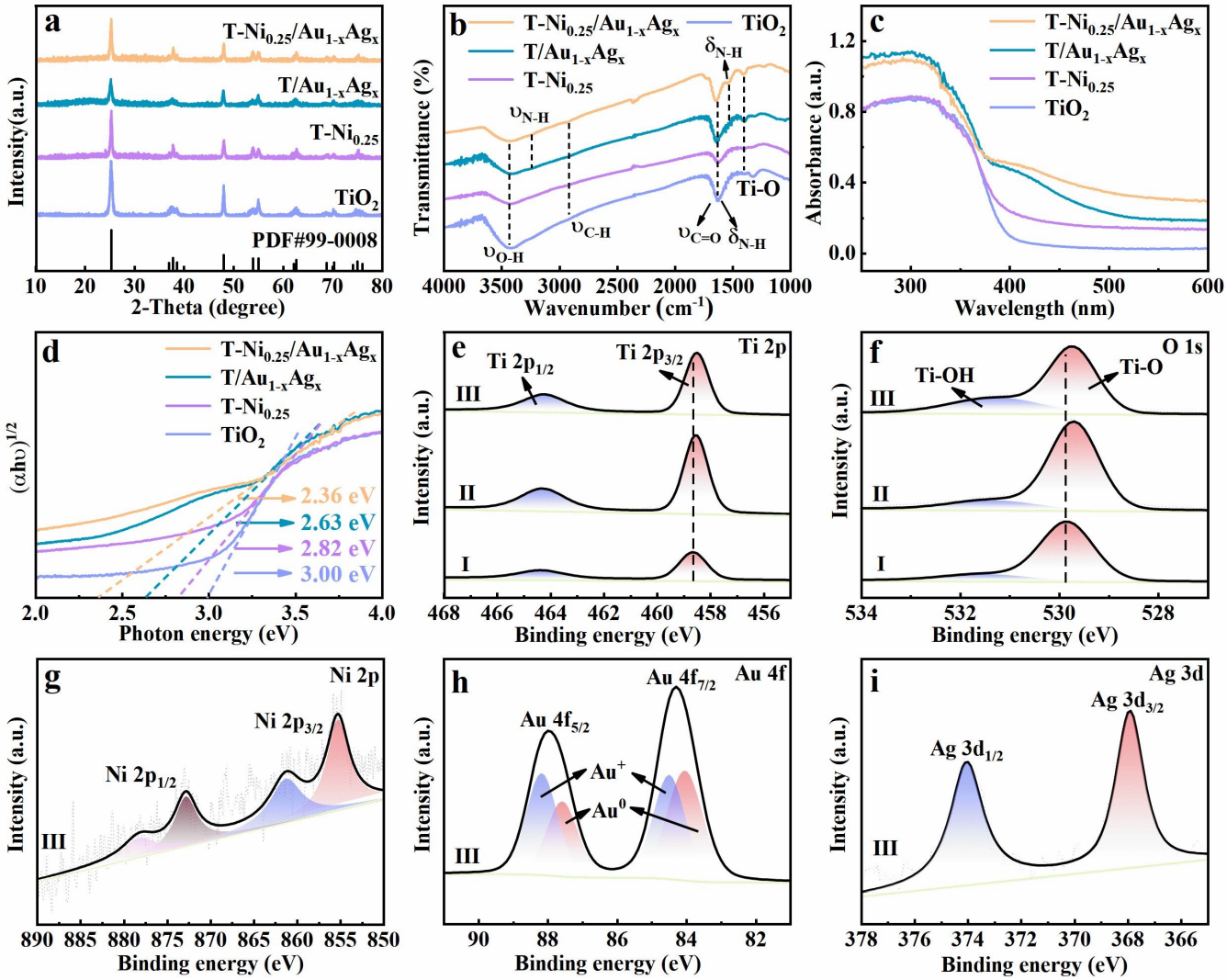

Figure 1. (a) XRD patterns and (b) FTIR spectra of pristine TiO_2, T-$Ni_{0.25}$, T/$Au_{1-x}Ag_x$ and T-$Ni_{0.25}$/$Au_{1-x}Ag_x$. (c) DRS results of pristine TiO_2, T-$Ni_{0.25}$, T/$Au_{1-x}Ag_x$ and T-$Ni_{0.25}$/$Au_{1-x}Ag_x$ with (d) transformed plots based on the Kubelka-Munk function vs. energy of light. High-resolution (e) Ti 2p, (f) O 1s, (g) Ni 2p, (h) Au 4f and (i) Ag 3d spectra of (I) pristine TiO_2, (II) T-$Ni_{0.25}$ and (III) T-$Ni_{0.25}$/$Au_{1-x}Ag_x$.

As shown in **Figure 1a**, all the XRD results of TiO_2, T-$Ni_{0.25}$, T/$Au_{1-x}Ag_x$, and T-$Ni_{0.25}$/$Au_{1-x}Ag_x$ exhibit the characteristic diffraction peaks at 25.3°, 37.8°, and 48.0°, corresponding to the (101), (004), and (200) crystal planes of anatase TiO_2 (JCPDS: 99-0008), respectively.[8] This observation confirms that Ni doping and $Au_{1-x}Ag_x$ NCs loading preserve the crystalline phase of TiO_2. The absence of distinct diffraction peaks of $Au_{1-x}Ag_x$ NCs or metallic Ni species can be attributed to their low content and high dispersion in the nanocomposite. Raman results (**Figure S5**) further corroborate the anatase phase of TiO_2, with no observable signals for Au_{1-}

View Article Online
DOI: 10.1039/D6SC02262F

$_xAg_x$ NCs or Ni dopant, aligning with the XRD results. It should be emphasized that the significant enhancement of the Eg peak intensity observed after Ni doping can be attributed to a surface-enhanced resonance Raman scattering (SERRS) effect.[2a, 14]

Fourier transform infrared (FTIR) spectroscopy (**Figure 1b** and **Table S1**) results of all the samples reveal an apparent peak at 1390 cm^{-1}, which is assigned to the Ti–O vibrational modes.[15] Particularly, $T/Au_{1-x}Ag_x$ and $T\text{-}Ni_{0.25}/Au_{1-x}Ag_x$ exhibit the additional peaks at 1640, 1530, 3241, and 2925 cm^{-1}, corresponding to the C=O, N–H, and C–H functional groups derived from the GSH ligands stabilizing the $Au_{1-x}Ag_x$ NCs.[16] These features strongly confirm the successful deposition of $Au_{1-x}Ag_x$ NCs on the TiO_2 substrate.

Diffuse reflectance spectroscopy (DRS) results (**Figures 1c & d**) demonstrate that the incorporation of $Au_{1-x}Ag_x$ NCs and Ni doping significantly enhance the visible-light harvesting capacity of TiO_2. The optical absorption edge of pristine TiO_2 is located in the ultraviolet light region of approximately 400 nm, corresponding to its intrinsic bandgap excitation.[17] According to the Kubelka-Munk function, E_g value of TiO_2 is determined to be approximately 3.00 eV. For the composite samples, E_g values of $T\text{-}Ni_{0.25}$, $T/Au_{1-x}Ag_x$, and $T\text{-}Ni_{0.25}/Au_{1-x}Ag_x$ are determined as 2.82 eV, 2.63 eV and 2.36 eV, respectively. Note that E_g decreases with Ni-doping and $Au_{1-x}Ag_x$ NCs loading. Especially, $T/Au_{1-x}Ag_x$ and $T\text{-}Ni_{0.25}/Au_{1-x}Ag_x$ exhibit the substantially improved visible-light absorption intensity after $Au_{1-x}Ag_x$ NCs loading, primarily due to the photosensitization effect of $Au_{1-x}Ag_x$ NCs. In contrast, pure Ni-doping samples only marginally enhances the light absorption of TiO_2, implying that Ni acts as a co-catalyst rather than a light-harvesting component in the $T\text{-}Ni_{0.25}/Au_{1-x}Ag_x$ composite.

N_2 adsorption-desorption isotherms combined with Brunauer-Emmett-Teller (BET) and Barrett-Joyner-Halenda (BJH) analyses (**Figure S6** and **Table S3**) reveal the specific surface area and porosity of the samples. All the samples exhibit the type IV isotherms and hysteresis loops at relative pressures (P/P_0) of 0.8-1.0, indicative of the mesoporous structure.[8] The BET specific surface areas of TiO_2, $T\text{-}Ni_{0.25}$, $T/Au_{1-x}Ag_x$, and $T\text{-}Ni_{0.25}/Au_{1-x}Ag_x$ are determined as 86.63, 74.92, 42.95, and 40.51 $m^2 \cdot g^{-1}$, respectively. The decreased surface area of TiO_2 with Ni and $Au_{1-x}Ag_x$ NCs incorporation might stem from aggregation and pore filling, implying specific surface area does not contribute to the enhanced photoactivities of $T/Au_{1-x}Ag_x$, and $T\text{-}Ni_{0.25}/Au_{1-x}Ag_x$ heterostructures. Instead, atomic-scale dispersion of Ni in oxide state and BNCs deposition likely generate more surface reactive sites that are critical for charge transfer and catalytic activity.

View Article Online
DOI: 10.1039/D6SC02262F

X-ray photoelectron spectroscopy (XPS) was used to analyzed the surface composition and chemical bond states of pristine TiO_2, T-$Ni_{0.25}$, T/$Au_{1-x}Ag_x$ and T-$Ni_{0.25}$/$Au_{1-x}Ag_x$ (**Figure S7** and **Table S2**). For pure TiO_2, the peaks of Ti 2p (**Figure 1e**) at 458.6 and 464.4 eV correspond to the Ti^{4+} species, while the O 1s signals at 529.9 eV and 531.5 eV are assigned to the lattice oxygen and adsorbed oxygen, respectively.[18] As for T-$Ni_{0.25}$, the obvious shifts in the Ti 2p and O 1s binding energy (**Figure 1e & f**) relative to pure TiO_2 indicate the formation of strong Ni–O–Ti chemical bonds, confirming the covalent interaction between Ni species and the TiO_2 substrate. In contrast, T/$Au_{1-x}Ag_x$ displays no discernible shifts in the Ti 2p or O 1s signals compared with those of pure TiO_2 (**Figure S8**), suggesting that $Au_{1-x}Ag_x$ NCs are physically adsorbed without disrupting the TiO_2 lattice. For T-$Ni_{0.25}$/$Au_{1-x}Ag_x$, the peak shifts are dominated by the Ni–TiO_2 interaction, while $Au_{1-x}Ag_x$ NCs are only adsorbed on the surface of the Ni-doped TiO_2 and do not destroy the interaction between Ni species and TiO_2 substrate. The high-resolution Ni 2p spectrum of T-$Ni_{0.25}$/$Au_{1-x}Ag_x$ (**Figure 1g**) displays the characteristic peaks of Ni^{2+} at 855.3 eV, 861.3 eV, 872.9 eV, and 878.3 eV.[19] The Au 4f signal of T-$Ni_{0.25}$/$Au_{1-x}Ag_x$ heterostructure (**Figure 1h**) reveals a mixture of metallic Au (0) (84.1 eV and 87.6 eV) and oxidized Au (I) (84.5 eV and 88.2 eV) for $Au_{1-x}Ag_x$ NCs, while the Ag 3d peaks at 367.9 eV and 374.0 eV (**Figure 1i**) verify the presence of Ag (I) species,[2a] aligning with the BNCs composition. The XPS results of T-$Ni_{0.25}$/$Au_{1-x}Cu_x$ and T-$Ni_{0.25}$/$Au_{1-x}Pt_x$ are specifically provided in **Figure S9** and **Figure S10**, respectively. These XPS results confirm that Ni doping induces the atomic-scale interfacial bonding with TiO_2, facilitating the interfacial charge transfer, while $Au_{1-x}Ag_x$ NCs act as efficient visible-light absorbers through physical adsorption. The XPS results strongly substantiate the successful Ni ion doping and BNCs decoration in the ternary heterostructure. Moreover, the lack of structural disruption by the BNCs deposition ensures the integrity of the Ni–TiO_2 interaction, thereby forming the synergistic heterostructure critical for enhanced photocatalytic performance.

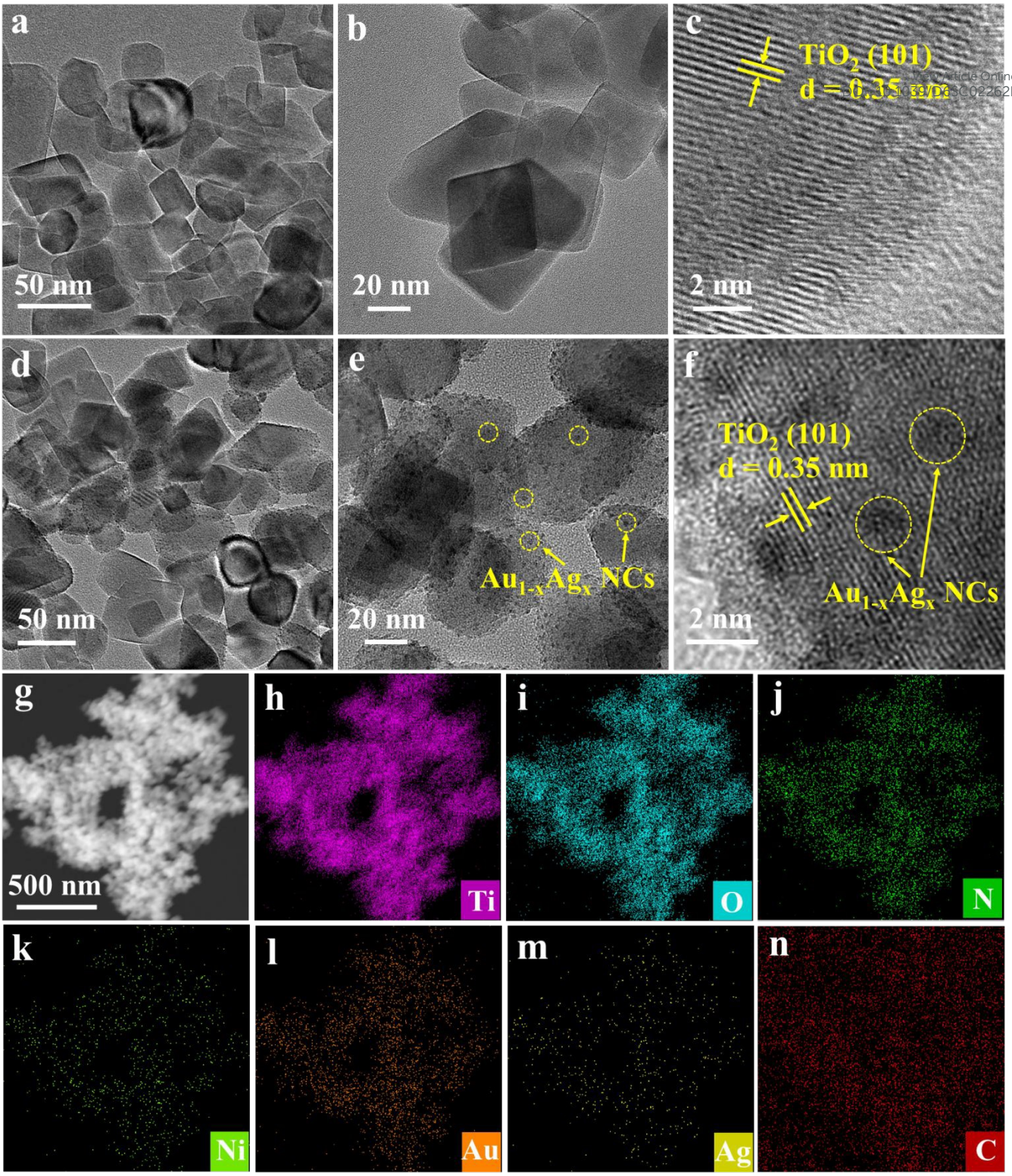

Figure 2. TEM and HRTEM images of (a-c) T-$Ni_{0.25}$, (d-f) T-$Ni_{0.25}/Au_{1-x}Ag_x$ with corresponding (g-n) elemental mapping results for (h) Ti, (i) O, (j) N, (k) Ni, (l) Au, (m) Ag, and (n) C signals.

As shown in **Figure 2a–f** and **Figure S11** at varying magnification reveal that all the samples maintain the two-dimensional (2D) nanosheet morphology of the TiO_2 substrate, suggesting that Ni doping and $Au_{1-x}Ag_x$ NCs loading do not alter the underlying architecture. As displayed in **Figure 2b & c** and **Figure S12**, TEM

View Article Online
DOI: 10.1039/D6SC02262F

and HRTEM images of pristine TiO_2 and T-$Ni_{0.25}$ exhibit the regular 2D nanosheet morphology with lateral dimension of 20-60 nm and a lattice spacing of 0.35 nm, corresponding to the (101) crystal plane of anatase TiO_2.[8] Critically, no distinct Ni nanoparticles or aggregates are observable in the TEM images of T-$Ni_{0.25}$ (**Figure 2a-c**), indicating that Ni is atomically dispersed or doped rather than forming bulk particles. In the TEM images of T-$Ni_{0.25}$/$Au_{1-x}Ag_x$ (**Figures 2d–f**), $Au_{1-x}Ag_x$ NCs appear as ultra-small size entities with a size of about 2 nm or less, uniformly distributed across the TiO_2 nanosheets without disrupting the crystalline structure of substrate.[20] This confirms that the electrostatic self-assembly process effectively anchors the $Au_{1-x}Ag_x$ NCs onto the Ni-doped TiO_2 nanosheets surface while preserving the nanosheet morphology. Energy-dispersive X-ray spectroscopy (EDS) mapping results (**Figure 2g–n**) of the T-$Ni_{0.25}$/$Au_{1-x}Ag_x$ composite material show homogeneous distributions of Ti, O, Ni, Au, and Ag elements, corroborating the XPS results aforementioned and once again providing the direct evidence for the successful incorporation of both Ni and $Au_{1-x}Ag_x$ NCs ingredients. The uniform dispersion of Ni dopant and $Au_{1-x}Ag_x$ NCs across the TiO_2 nanosheets underscores structural integrity of the heterostructure. This morphological and compositional characterization collectively establishes that the synthetic strategy achieves atomic-level dispersion of Ni dopant while achieving ultrafine clustering of $Au_{1-x}Ag_x$ NCs on the TiO_2 nanosheets, forming a well-defined heterostructure critical for efficient charge separation and photocatalytic activity.

3.2 Photocatalytic H_2 Generation Activities

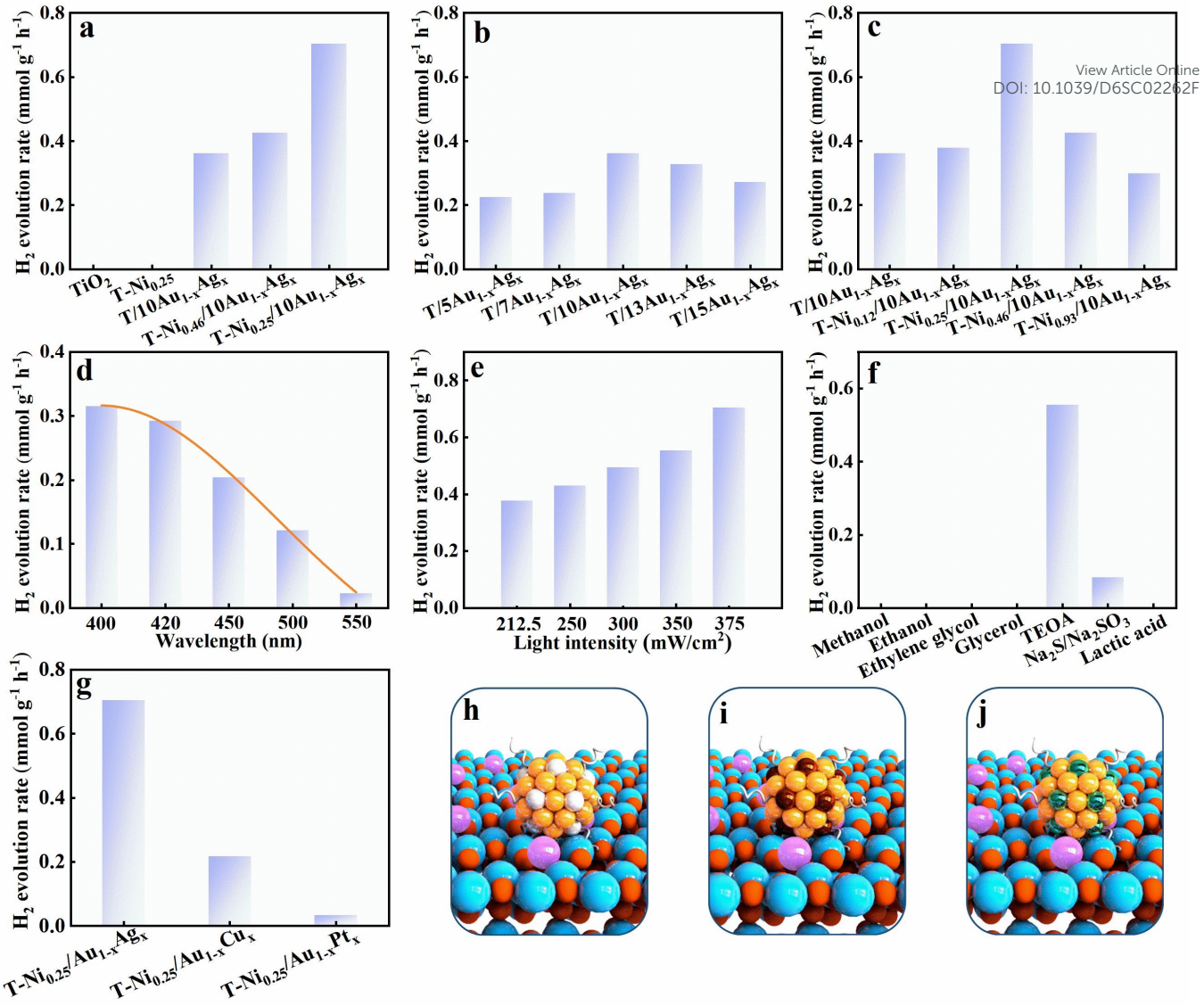

Figure 3. (a) Photoactivity comparison among pristine TiO_2, T-$Ni_{0.25}$, T/10$Au_{1-x}Ag_x$, T-$Ni_{0.46}$/10$Au_{1-x}Ag_x$ and T-$Ni_{0.25}$/10$Au_{1-x}Ag_x$ toward hydrogen generation under visible light ($\lambda > 420$ nm) irradiation. Photocatalytic H_2 evolution performances of TiO_2-Ni/$Au_{1-x}Ag_x$ with different (b) $Au_{1-x}Ag_x$ and (c) Ni loading amount under visible light ($\lambda > 420$ nm) irradiation. Photocatalytic H_2 evolution performances of T-$Ni_{0.25}$/10$Au_{1-x}Ag_x$ under (d) different monochromatic light irradiation, (e) light intensities and (f) sacrificial reagents. (g) Photoactivity comparison among T-$Ni_{0.25}$/$AuAg_{10}$, T-$Ni_{0.25}$/$AuCu_{10}$, and T-$Ni_{0.25}$/$AuPt_{10}$. Schematic diagram depicting the structures of (h) TiO_2-$Ni_{0.25}$/$Au_{1-x}Ag_x$, (i) TiO_2-$Ni_{0.25}$/$Au_{1-x}Cu_x$ and (j) TiO_2-$Ni_{0.25}$/$Au_{1-x}Pt_x$.

Using tri-ethanolamine (TEOA) as a hole-trapping agent, photocatalytic hydrogen evolution activities of the samples were systematically evaluated under visible light irradiation ($\lambda > 420$ nm). As shown in **Figure 3a**, pristine TiO_2 exhibited no hydrogen production activity under visible light, attributed to its wide bandgap which precludes the band-gap-photoexcitation.[21] Upon doping of Ni, photocatalytic hydrogen evolution

View Article Online
DOI: 10.1039/D6SC02262F

activity of T-$Ni_{0.25}$ remains undetectable, indicating that Ni doping alone cannot confer TiO_2 with visible-light responsiveness, which agrees with the DRS result. In contrast, T/10$Au_{1-x}Ag_x$, T-$Ni_{0.46}$/10$Au_{1-x}Ag_x$, and T-$Ni_{0.25}$/10$Au_{1-x}Ag_x$ display measurable hydrogen production, implying that $Au_{1-x}Ag_x$ NCs act as efficient photosensitizers, extending the photo-response range of TiO_2 to the visible spectrum. The enhanced photocatalytic performance of T-$Ni_{0.46}$/10$Au_{1-x}Ag_x$ compared with T/10$Au_{1-x}Ag_x$ strongly highlights the critical role of Ni doping as a co-catalyst in accelerating the interfacial electron transfer, thereby improving the charge separation efficiency.[9] Optimization of $Au_{1-x}Ag_x$ NCs loading (**Figure 3b**) revealed that T/10$Au_{1-x}Ag_x$ with 10 mL of BNCs exhibited the highest hydrogen evolution rate of 0.36 mmol·g^{-1}·h^{-1}, reflecting the optimal balance between light absorption and charge transport.[22] Further tuning of Ni doping levels (**Figure 3c**) suggests that the T-$Ni_{0.25}$/10$Au_{1-x}Ag_x$ containing 0.25 wt%-Ni and 10 mL of $Au_{1-x}Ag_x$ NCs achieved a significantly higher hydrogen evolution rate of 0.70 mmol·g^{-1}·h^{-1}, establishing this as the optimal catalyst for subsequent systematic investigation.

Inductively coupled plasma-mass spectrometry (ICP-MS) was employed to quantitatively determine the true amount of $Au_{1-x}Ag_x$ NCs and Ni dopant in the T-$Ni_{0.25}$/10$Au_{1-x}Ag_x$ heterostructure. As summarized in **Table S4**, loading percentage of $Au_{1-x}Ag_x$ NCs and Ni dopant in the T-$Ni_{0.25}$/10$Au_{1-x}Ag_x$ is approximately 3.83 and 0.09 wt%, respectively. This result signifies that even a low amount of Ni dopant surprisingly yielded a substantial enhancement in photoactivity, underscoring the critical role of Ni dopants as co-catalysts in facilitating the interfacial electron transfer. Monochromatic light irradiation tests (**Figure 3d**) revealed that the photocatalytic hydrogen evolution performance of T-$Ni_{0.25}$/10$Au_{1-x}Ag_x$ decreases with increasing wavelength in the visible range, with the highest activity observed under near-ultraviolet light (λ = 400 ~ 420 nm). This wavelength dependence aligns with the DRS results, confirming that while $Au_{1-x}Ag_x$ NCs broaden the light absorption of TiO_2, the absorption efficiency remains primarily confined to the short-wavelength visible region. Light intensity measurements (**Figure 3e**) show a linear increase in photocatalytic hydrogen production rate with increasing light intensity, indicating that the photoreaction system operates under photon-limited conditions and possesses untapped potential for enhanced performance under higher irradiance, verifying it is indeed a photocatalytic reaction. Photocatalytic experiments with adding different sacrificial agents (**Figure 3f**) demonstrate that TEOA outperformed other hole scavengers (methanol, ethanol, ethylene glycol, glycerol, lactic acid, and Na_2S/Na_2SO_3), yielding the highest hydrogen evolution activity. This superiority is attributed to the suitable redox potential and strong hole-trapping ability of TEOA, facilitated

View Article Online
DOI: 10.1039/D6SC02262F

by its tertiary amine group, which efficiently scavenges photogenerated holes and promotes sustained electron transfer to the catalyst surface, ultimately boosting the hydrogen generation.[23] The chemical structure and redox properties of sacrificial agent are critical determinants of catalytic performance, underscoring the importance of system-wide optimization in photocatalytic hydrogen production. As displayed in **Figure S13**, cyclic stability tests indicate that photoactivity of the T-$Ni_{0.25}$/10$Au_{1-x}Ag_x$ heterostructure exhibits the apparent decay after the 2nd cyclic reaction. The relatively unfavorable cycling performance of the T-$Ni_{0.25}$/10$Au_{1-x}Ag_x$ heterostructure is likely attributed to the vigorous stirring during continuous photocatalytic reactions, which causes the detachment of $Au_{1-x}Ag_x$ NCs from the TiO_2 substrate, thereby weakening the visible-light absorption capacity of the composite and diminishing the number of active sites available for catalysis. More importantly, the intrinsic poor stability of metal NCs cannot be ignored, which makes the gradual *in-situ* transformation of metal NCs to conventional metal nanocrystals under continuous light irradiation, hence losing the advantageous photosensitization effect of metal NCs. Nevertheless, photocatalytic performance enhancement significantly implies that the synergistic combination of $Au_{1-x}Ag_x$ NCs as photosensitizers and Ni doping as a co-catalyst enables efficient visible-light-driven hydrogen evolution by expanding the spectral response of TiO_2 and optimizing charge carrier dynamics. To further assess the generality of this strategy, a series of other alloy NCs-based T-$Ni_{0.25}$/[$Au_{1-x}Cu_x$, $Au_{1-x}Pt_x$] heterostructures were prepared using the analogous methodologies for visible-light-driven photocatalytic hydrogen production. The related characterizations of T-$Ni_{0.25}$/[$Au_{1-x}Cu_x$, $Au_{1-x}Pt_x$] heterostructures are specifically provided in **Figure S9** and **Figure S10**. As shown in **Figure 3g**, T-$Ni_{0.25}$/$Au_{1-x}Ag_x$ heterostructure consistently exhibits the highest photoactivity among the tested systems under visible-light irradiation. Notably, all these alloy NCs-modified samples (**Figure 3h−j**) extend the light absorption spectrum of the TiO_2 substrate to the visible region and demonstrate measurable photocatalytic activities, collectively highlighting the universal applicability of $Au_{1-x}Ag_x$, $Au_{1-x}Cu_x$, and $Au_{1-x}Pt_x$ NCs as photosensitizers in this heterostructure design.

3.3 PEC and spectroscopic analysis

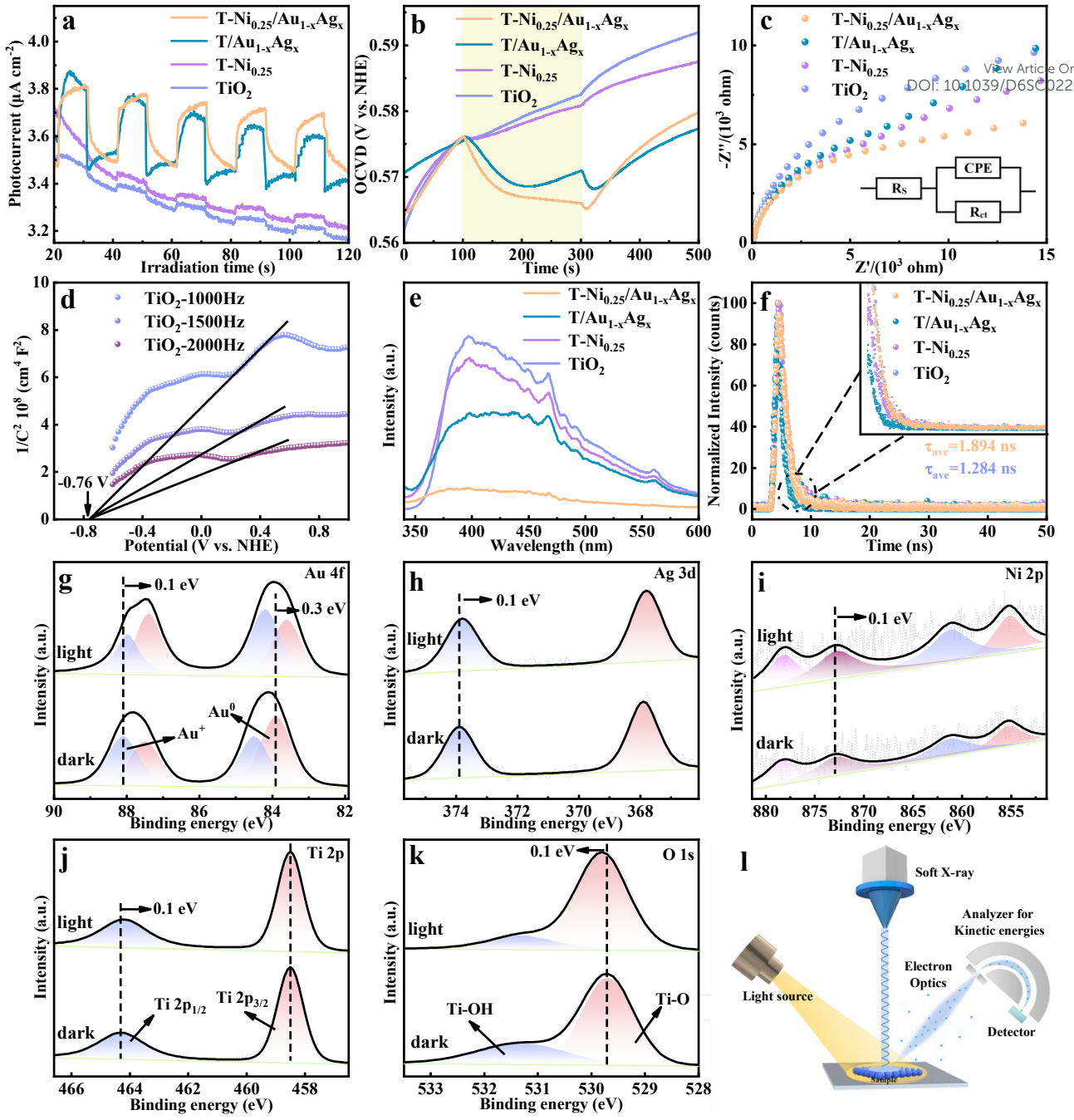

Figure 4. (a) Photocurrents, (b) open-circuit voltage decay (OCVD), and (c) EIS Nyquist plots of pristine TiO_2, T-$Ni_{0.25}$, T/$Au_{1-x}Ag_x$ and T-$Ni_{0.25}$/$Au_{1-x}Ag_x$ under visible light (λ > 420 nm) irradiation, for which aqueous Na_2SO_4 solution (0.5 M, pH = 6.69) was utilized as the electrolyte. (d) Mott-Schottky plots of TiO_2 under different frequencies. (e) PL spectra and (f) time-resolved transient PL decay of pristine TiO_2, T-$Ni_{0.25}$, T/$Au_{1-x}Ag_x$ and T-$Ni_{0.25}$/$Au_{1-x}Ag_x$. *In-situ* irradiated XPS high-resolution (g) Au 4f, (h) Ag 3d, (i) Ni 2p, (j) Ti 2p and (k) O 1s spectra of T-$Ni_{0.25}$/$Au_{1-x}Ag_x$ with and without light irradiation (λ > 420 nm). (l) Schematic diagram of *in-situ* irradiated XPS for probing high-resolution spectra.

View Article Online
DOI: 10.1039/D6SC02262F

To elucidate the impact of BNCs deposition and Ni doping on the interfacial charge separation efficiency of the T-$Ni_{0.25}/Au_{1-x}Ag_x$ artificial photosystem, a comprehensive set of photoelectrochemical (PEC) analyses were performed on each photocatalyst. Transient photocurrent response is regarded as the most intuitive method for evaluating the carrier separation efficiency of photoelectrodes.[24] **Figure 4a** shows the periodic on/off transient photocurrent responses of pristine TiO_2, T-$Ni_{0.25}$, T/$Au_{1-x}Ag_x$, and T-$Ni_{0.25}/Au_{1-x}Ag_x$ heterostructure under intermittent visible light irradiation ($\lambda > 420$ nm). Notably, photocurrent density of T-$Ni_{0.25}/Au_{1-x}Ag_x$ is significantly higher than that of pristine TiO_2. Careful observation reveals that since TiO_2 is a wide bandgap semiconductor and it cannot be photoexcited under visible light, and thus it generates almost no photocurrent. Moreover, after the introduction of Ni co-catalyst, the increase in the photocurrent density of T-$Ni_{0.25}$ is still relatively small since Ni doping fails to alter the light absorption of TiO_2 substrate, as unveiled by the DRS result. However, after loading the $Au_{1-x}Ag_x$ NCs, both T/$Au_{1-x}Ag_x$ and T-$Ni_{0.25}/Au_{1-x}Ag_x$ generate apparent photocurrents under visible light, which strongly indicates that $Au_{1-x}Ag_x$ NCs serve as effective photosensitizers. The photocurrent improvement of T-$Ni_{0.25}/Au_{1-x}Ag_x$ compared with T/$Au_{1-x}Ag_x$ indicates that the Ni doping can indeed accelerate the interfacial electron transport, thereby enhancing the carrier separation efficiency, which is consistent with the aforementioned photocatalytic performance analysis. To explore the charge recombination dynamics, open-circuit photovoltage decay (OCVD) results of the photoanodes were studied, which is regarded as an effective tool to monitor the open-circuit voltage (V_{oc}) decay when the light is turned off in a stable state.[25] As shown in **Figure 4b**, TiO_2 and T-$Ni_{0.25}$ show almost no voltage attenuation owing to large bandgap for negligible visible light absorption, while T-$Ni_{0.25}/Au_{1-x}Ag_x$ exhibits the maximum photovoltage, which once again confirms that simultaneous introduction of $Au_{1-x}Ag_x$ and Ni doping leads to the most enhanced charge separation. Similarly, this result is completely consistent with the result of the transient photocurrent response. Alternatively, **Figure 4c** and **Table S5** shows the electrochemical impedance spectroscopy (EIS) results of the different samples under visible light irradiation. Among them, T-$Ni_{0.25}/Au_{1-x}Ag_x$ shows the minimum semi-circular arc radius, indicating that $Au_{1-x}Ag_x$ NCs loading and Ni doping effectively reduce the interfacial charge transfer resistance of the heterostructure. Therefore, PEC results strongly validate that the significant improvement in the photoactivity of T-$Ni_{0.25}/Au_{1-x}Ag_x$ is primarily attributed to the synergistic promotion of charge separation and migration afforded by Ni doping and $Au_{1-x}Ag_x$ NCs photosensitization. According to the M-S results of TiO_2, T-$Ni_{0.25}$, T/$Au_{1-x}Ag_x$ and T-$Ni_{0.25}/Au_{1-x}Ag_x$ (**Figure S14**), T-$Ni_{0.25}/Au_{1-x}Ag_x$ exhibits the largest charge carrier density (3.5×10^{19} cm^{-3}), confirming the key role of Ni doping and $Au_{1-x}Ag_x$ decoration in accelerating the interfacial charge

View Article Online
DOI: 10.1039/D6SC02262F

separation. Overall, the results of photocurrent, OCVD, EIS, M-S and N_D are consistent with the photocatalytic performances. In addition, according to the UV-vis absorption spectra (**Figure S1e**) and cyclic voltammetry (CV) results (**Figure S15**), the highest occupied molecular orbital (HOMO) and the lowest unoccupied molecular orbital (LUMO) levels of $Au_{1-x}Ag_x$ NCs are determined to be approximately -2.235 V and 0.655 V vs. NHE (**Figure S18a**), respectively. The HOMO and LUMO levels of $Au_{1-x}Cu_x$ and $Au_{1-x}Pt_x$ NCs were also determined by the analogous methods (**Figure S16-S18**).

To elucidate the photocatalytic mechanism, charge transport processes in TiO_2, T-$Ni_{0.25}$, T/$Au_{1-x}Ag_x$ and T-$Ni_{0.25}$/$Au_{1-x}Ag_x$ were studied spectroscopically. Photoluminescence (PL) spectroscopy was employed to analyze the carrier recombination efficiency. As shown in **Figure 4e**, steady-state PL spectra of the samples were recorded under 360 nm excitation. All the composite samples exhibit lower PL intensities compared with pure TiO_2, indicating that Ni doping and $Au_{1-x}Ag_x$ NCs photosensitization significantly suppress the electron-hole pairs recombination. Among them, T-$Ni_{0.25}$/$Au_{1-x}Ag_x$ shows the lowest PL intensity, signifying its maximally suppressed carrier recombination and the optimal charge separation. Time-resolved photoluminescence (TRPL) decay curve spectroscopy was used to probe the carrier dynamics of the photosystems. The fitting results (**Figure 4f** & **Table S6**) reveal that the average lifetime of the optimal sample T-$Ni_{0.25}$/$Au_{1-x}Ag_x$ is 1.894 ns, compared with 1.598 ns for pristine TiO_2. The extended average lifetime of T-$Ni_{0.25}$/$Au_{1-x}Ag_x$ indicates a reduction in radiative recombination, suggesting an increased availability of carriers for the photocatalytic reaction. These results collectively demonstrate that concurrent Ni doping and $Au_{1-x}Ag_x$ NCs loading synergistically inhibit the carrier recombination. Comparative analysis of the photoactivities, PEC performances and PL results (**Figures 4a-f**) between T/$Au_{1-x}Ag_x$ and T-$Ni_{0.25}$/$Au_{1-x}Ag_x$ further confirms that Ni doping enhances the overall performances of the samples. We speculate that the Ni dopant acts as an efficient electron transfer mediator, facilitating the unidirectional and smooth electron flow from $Au_{1-x}Ag_x$ NCs to the TiO_2 substrate, thereby validating its role as a co-catalyst.

In-situ XPS characterization, a powerful technique to analyze the surface chemistry and charge transport mechanisms of photocatalysts, was also performed.[26] The changes in the binding energy of core elements directly reflect the variation in electron density. As illustrated in **Figure 4g-i**, obvious shifts in the binding energies of Au 4f, Ag 3d, and Ni 2p for the T-$Ni_{0.25}$/$Au_{1-x}Ag_x$ composite were observed under visible light irradiation compared with the dark-state conditions. These shifts verify the occurrence of photoelectron transfer upon light exposure, providing crucial evidence for determining the charge transfer pathways of the

composite materials under visible light irradiation. Specifically, as TiO_2 is inactive under visible light, photoelectrons generated in the $Au_{1-x}Ag_x$ NCs migrate to the TiO_2 substrate, and Ni dopant functioning as co-catalyst accelerates electrons migration process. This is rationalized by the blue-shift in the binding energies of Ti 2p and O 1s for T-$Ni_{0.25}$/$Au_{1-x}Ag_x$ heterostructure (**Figure 4j-k**). Noteworthily, the reduced binding energy of Ni 2p for T-$Ni_{0.25}$/$Au_{1-x}Ag_x$ heterostructure upon light irradiation also indicates the electron flow from $Au_{1-x}Ag_x$ NCs to Ni dopant that acts as interfacial electron transport mediator (**Figure 4i**).

View Article Online
DOI: 10.1039/D6SC02262F

3.4 Photocatalytic mechanism

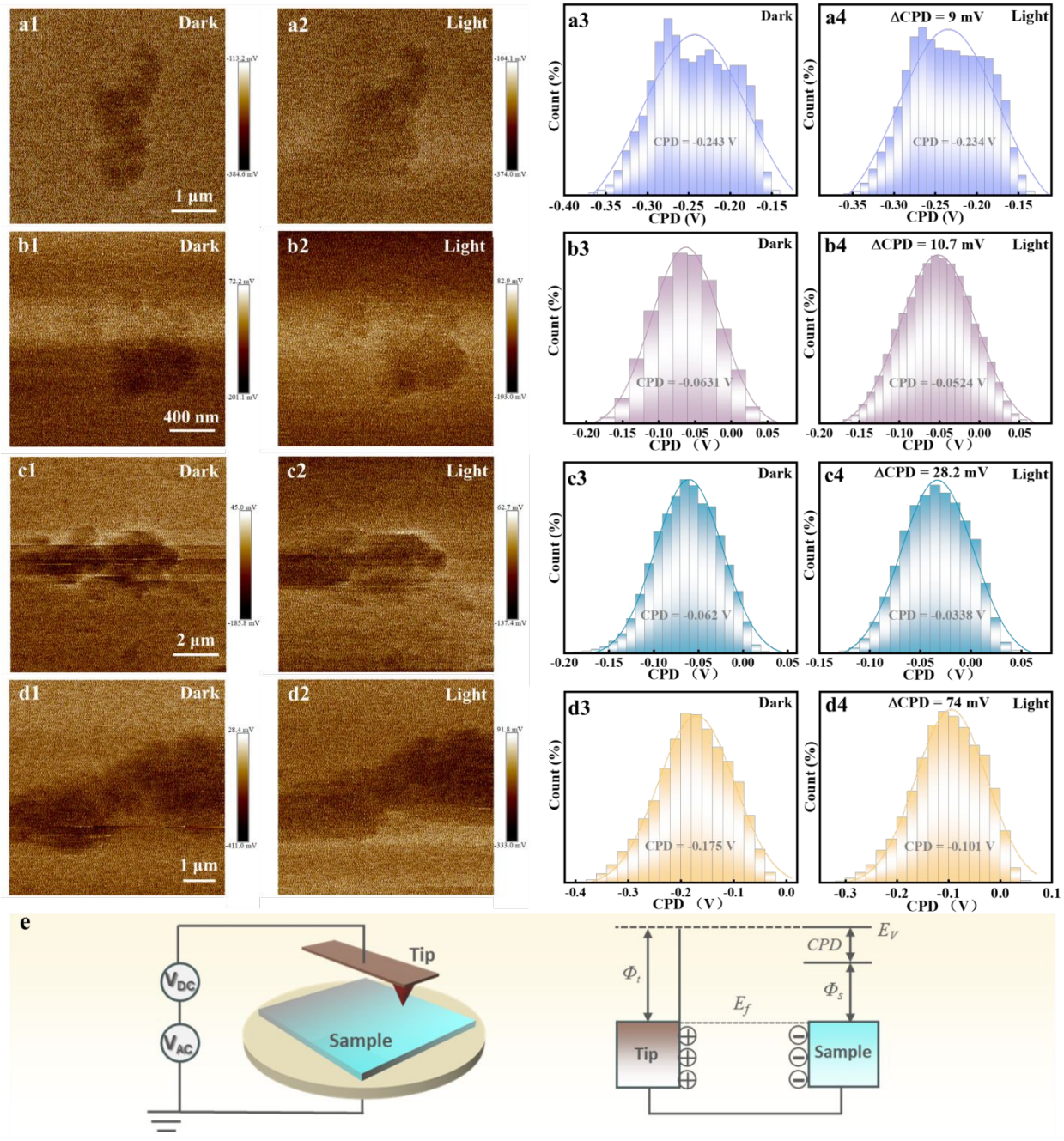

Figure 5. KPFM images of (a) pristine TiO_2, (b) T-$Ni_{0.25}$, (c) T/$Au_{1-x}Ag_x$ and (d) T-$Ni_{0.25}$/$Au_{1-x}Ag_x$ (a1-d1) in

the dark conditions and (a2-d2) under visible light irradiation. Corresponding surface contact potential distributions (CPD) of pristine TiO_2, T-$Ni_{0.25}$, T/$Au_{1-x}Ag_x$ and T-$Ni_{0.25}$/$Au_{1-x}Ag_x$ (a3-d3) in the dark conditions and (a4-d4) under visible light irradiation. (e) Schematic illustration of CPD determination by KPFM measurement on sample surface.

View Article Online
DOI: 10.1039/D6SC02262F

To deeply investigate the photogenerated charge separation behavior, Kelvin probe force microscopy (KPFM) was employed to obtain high-resolution nanoscale images of surface morphology and potential. KPFM operates based on the work function difference between the probe and the sample.[27] Upon contact, electron flow equilibrates their Fermi levels, producing a contact potential difference (CPD) that depends on both the probe work function (Φ_t) and the sample work function (Φ_s), as shown in **Figure 5e**.[28] Thus, variations in CPD directly reveal the distribution and separation of charge carriers on the sample surface.[29] **Figure S20** & **Figure 5** present the surface morphologies and potential images of all the samples. As shown in **Figure 5a1-d1**, pristine TiO_2, T-$Ni_{0.25}$, T/$Au_{1-x}Ag_x$ and T-$Ni_{0.25}$/$Au_{1-x}Ag_x$ exhibit non-uniform potential distribution across the scanned region, and difference in CPD before and after visible light irradiation (**Figure 5a2-d2**) is clearly visible through color contrast in the potential maps. Under visible light illumination conditions, photogenerated electron-hole pairs separate, leading to an increase in CPD for all the samples. The corresponding ΔCPD values for pure TiO_2, T-$Ni_{0.25}$, T/$Au_{1-x}Ag_x$ and T-$Ni_{0.25}$/$Au_{1-x}Ag_x$ are determined as 9 mV, 10.7 mV, 28.2 mV, and 74 mV, respectively (**Figures 5a3-d3 & a4-d4**). The positive ΔCPD indicates greater holes accumulation on the surface after light illumination, meaning the surface potential change is primarily governed by holes.[30] Comparisons reveal that the ΔCPD changes of pure TiO_2 and T-$Ni_{0.25}$ are relatively small. In contrast, after depositing $Au_{1-x}Ag_x$ NCs, both T/$Au_{1-x}Ag_x$ and T-$Ni_{0.25}$/$Au_{1-x}Ag_x$ exhibit significantly enhanced ΔCPD, with the latter showing the most pronounced increase. This suggests that T-$Ni_{0.25}$/$Au_{1-x}Ag_x$ accumulates more photogenerated charges on the surface under visible light illumination.[31] Additionally, the CPD line-scan profiles (**Figure S21a4-d4**) further verify this trend, that is, T-$Ni_{0.25}$/$Au_{1-x}Ag_x$ displays the largest CPD enhancement, strongly confirming its more efficient directional exciton transfer and improved spatial separation of electron-hole pairs. These findings align with the PEC results, jointly confirming that the superior photogenerated charge separation and transfer capability of T-$Ni_{0.25}$/$Au_{1-x}Ag_x$ heterostructure.

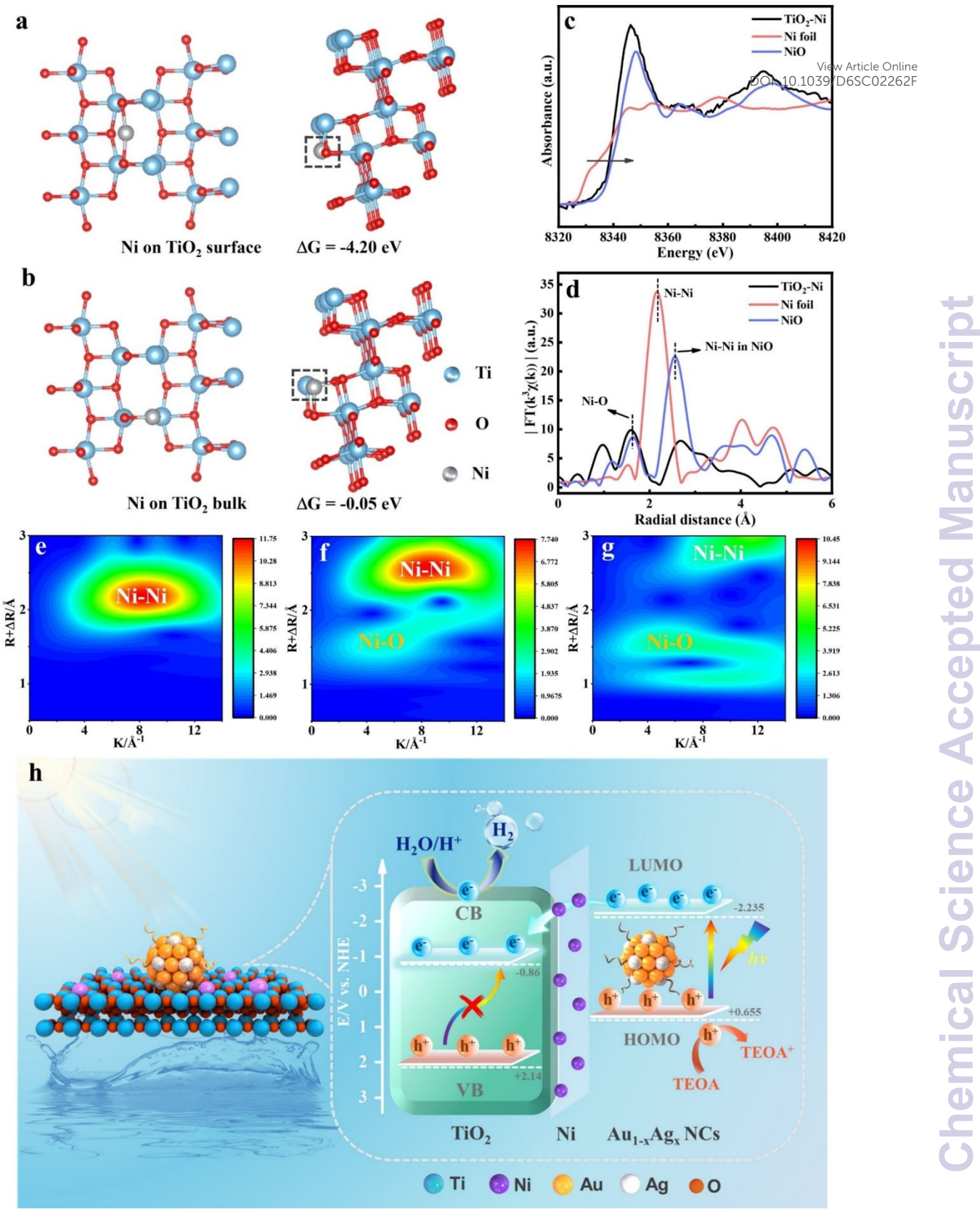

Figure 6. The molecular models of Ni (a) on the surface and (b) in the bulk of TiO_2. (c) XANES and (d) EXAFS spectra of TiO_2-Ni. Wavelet transform (WT) for the EXAFS signals of (e) Ni foil, (f) NiO and (g) TiO_2-Ni. (h) Schematic illustration of the photocatalytic mechanism of T-$Ni_{0.25}$/$Au_{1-x}Ag_x$ heterostructure.

View Article Online
DOI: 10.1039/D6SC02262F

Elucidating the modulation of the electronic structure and atomic coordination environment of the doped Ni species in TiO_2 is crucial for understanding the photocatalytic mechanism of T-$Ni_{0.25}/Au_{1-x}Ag_x$ heterostructure. Density functional theory (DFT) calculations were performed to determine the preferential location of Ni species in the TiO_2 substrate. As shown in **Figure 6a**, the configuration where Ni adsorbs on the TiO_2 surface, forming direct Ni–O bonds, yields a binding energy of -4.20 eV. In contrast, the substitution of Ni at Ti sites in the TiO_2 bulk results in a binding energy of only -0.05 eV. The significantly more negative binding energy for surface adsorption indicates that this configuration is energetically far more favorable. This computational conclusion is consistent with EXAFS results below, which suggests the formation of Ni–O bonds on the TiO_2 surface rather than replacement of Ti atoms with Ni.

The Ni doping of TiO_2 by the MSM method, enabled by high-temperature conditions, facilitates Ni-O bond formation between freely mobile Ni^{2+} ions and surface oxygen ions of TiO_2, as corroborated by extended X-ray absorption fine structure (EXAFS) and X-ray absorption near-edge structure (XANES) spectroscopy (**Figures 6a & b**). As shown in **Figure 6b**, absorption edge of TiO_2-Ni is positioned closer to that of NiO than to metallic Ni foil, indicating that the valence state of Ni in TiO_2-Ni lies between +1 and +2, closely approaching the +2 state.[32] Ni K-edge R-space EXAFS analysis (**Figure 6c**) of TiO_2-Ni reveals two characteristic peaks at 1.6 Å and 2.6 Å which is analogous to that of NiO, corresponding to the Ni-O and Ni-Ni coordinate ion bonds, respectively.[33] As shown in **Table S7**, the fitting results of the EXAFS data are specifically summarized. Notably, the absence of the Ni-Ni bonding peak of metallic Ni foil within the TiO_2-Ni spectrum indicates that Ni elements are dispersed rather than forming metallic atoms, strongly suggesting their existence in an oxidized state.[34] Additionally, wavelet transform (WT) analysis of the EXAFS spectra was performed to verify the atomic dispersion (**Figure 6e-g**). In comparison with the WT profiles of Ni foil and NiO, TiO_2-Ni exhibits two obvious coordination at approximately 5 $Å^{-1}$ and 9 $Å^{-1}$, corresponding to the Ni–O and Ni–Ni coordination, respectively. This indicates that the Ni species on TiO_2-Ni are in an oxidized state, which is consistent with the EXAFS results. Collectively, these results provide unambiguous evidence for the successful doping of Ni onto the TiO_2 surface, with the formation of Ni-O surface linkages critical for modulating the electronic structure of the semiconductor.

Based on the M-S results (**Figure 4d**), conduction band (CB) potential (E_{CB}) of TiO_2 was determined to be -0.76 V relative to NHE (-0.34 V relative to RHE), and considering the E_{fb} of n-type semiconductor is more positive by 0.1 V than the E_{CB}, E_{CB} of TiO_2 is calibrated to be -0.86 V vs. NHE. Given that the bandgap of

View Article Online
DOI: 10.1039/D6SC02262F

TiO_2 determined from the DRS results is 3.00 eV (**Figure 1d**), valence band (VB) level of TiO_2 can thus be calculated as 2.14 eV relative to NHE. Based on the experimental analyses, a photocatalytic mechanism is proposed, as illustrated in **Figure 6h**. When the T-$Ni_{0.25}$/$Au_{1-x}Ag_x$ heterostructure is irradiated with visible light, $Au_{1-x}Ag_x$ NCs undergo photoexcitation, inducing electron transitions from the HOMO to the LUMO level. Owing to the favorable energy level alignment between the LUMO level of $Au_{1-x}Ag_x$ NCs and the CB of TiO_2, photoexcited electrons in the LUMO level of $Au_{1-x}Ag_x$ NCs rapidly inject into the CB of TiO_2 substrate, establishing a direct charge transfer pathway. The Ni species doped on the TiO_2 surface function as co-catalyst via strong Ni−O chemical bonding which plays dual roles by lowering the energy barrier for electron transfer from $Au_{1-x}Ag_x$ NCs to TiO_2 through modulating the interfacial electronic structure and constructing a cascaded electron transport pathway, thereby accelerating the directional charge migration. This Ni-mediated synergy significantly suppresses the electron-hole recombination and enhances the separation efficiency of photogenerated charge carriers over $Au_{1-x}Ag_x$ NCs.[9, 35] Subsequently, the transferred electrons accumulate at the TiO_2 surface and then react with protons (H^+) adsorbed at the active sites of TiO_2 surface to drive the hydrogen evolution reaction. The discrete energy levels of BNCs combined with the uniform dispersion of Ni co-catalysts, create a robust "light absorption-charge separation-proton reduction" cascade charge transfer channel, enabling efficient conversion of solar energy into chemical energy. The synergy between molecular-like BNCs as light-harvesting units and Ni co-catalyst as charge-accelerating nodes represents a rational design strategy for constructing high-performance heterostructure photocatalysts, providing a foundational framework for advancing solar-to-hydrogen conversion technologies.

The TiO_2-Ni/alloy NCs demonstrate a more superior photocatalytic mechanism compared to traditional semiconductor photocatalysts and metal nanoparticles. Conventional semiconductor photocatalysts generate electron-hole pairs by interband transitions but are often constrained by limited visible-light response and rapid carrier recombination[36]. Metal nanoparticles can contribute via plasmonic effects or hot-electron injection, yet their function is typically confined to isolated steps[37]. In contrast, metal NCs possess a discrete electronic structure with both molecule-like and nanomaterial-like characteristics, enabling more versatile light absorption and charge transfer pathways. Furthermore, BNCs allow compositional tuning to optimize energy-level alignment with the semiconductor. In this work, BNCs form a favorable cascade alignment with TiO_2-Ni, promoting efficient electron transition, suppressing charge recombination, and prolonging excited-state carrier lifetimes.

4. Conclusions

View Article Online
DOI: 10.1039/D6SC02262F

To sum up, TiO_2-Ni/alloy NCs ($Au_{1-x}Ag_x$, $Au_{1-x}Pt_x$, $Au_{1-x}Cu_x$) heterostructures were fabricated by a facile and universal molten salt method combined with an electrostatic self-assembly strategy. The results confirm that BNCs ($Au_{1-x}Ag_x$, $Au_{1-x}Pt_x$, $Au_{1-x}Cu_x$) decoration extends the light absorption of TiO_2 to the visible region, meanwhile Ni doping accelerates the interfacial charge transport, thus synergistically boosting the electron separation from BNCs to TiO_2. This synergy significantly enhanced the visible-light-driven photocatalytic hydrogen evolution performances of TiO_2-Ni/alloy NCs ($Au_{1-x}Ag_x$, $Au_{1-x}Pt_x$, $Au_{1-x}Cu_x$) heterostructures by virtue of their favorable energy level alignment. Furthermore, charge transfer mechanism of TiO_2-Ni/alloy NCs artificial photosystems was unraveled, revealing a synergistic effect between atomic-scale metal NCs and metal oxide supports.

Data availability

All data supporting the findings of this study are available within the paper and its supplementary information files. Source data are provided with this paper.

Competing interests

The authors declare no competing interests.

Acknowledgements

The support by the award Program for Minjiang scholar professorship is greatly acknowledged. This work was financially supported by the National Natural Science Foundation of China (No. 21703038, 22072025). The financial supports from state key laboratory of structural chemistry, Fujian institute of research on the structure of matter, Chinese academy of science (No. 20240018), and Natural Science Foundation of Fujian Province (2024J01263) are acknowledged.

References

[1] a) R. C. Jin, C. J. Zeng, M. Zhou, Y. X. Chen, *Chem. Rev.* **2016**, *116*, 10346-13413; b) I. Chakraborty, T. Pradeep, *Chem. Rev.* **2017**, *117*, 8208-8271; c) X. Kang, Y. W. Li, M. Z. Zhu, R. C. Jin, *Chem. Soc.*

Rev. **2020**, *49*, 6443-6514; d) L. C. Liu, A. Corma, *Chem. Rev.* **2018**, *118*, 4981-5079; e) Y. X. Du, H. T. Sheng, D. Astruc, M. Z. Zhu, *Chem. Rev.* **2020**, *120*, 526-622.

View Article Online
DOI: 10.1039/D6SC02262F

[2] a) Q. L. Mo, B. J. Liu, F. X. Xiao, *J. Phys. Chem. C* **2021**, *125*, 22421-22428; b) L. P. Zhang, J. R. Ran, S. Z. Qiao, M. Jaroniec, *Chem. Soc. Rev.* **2019**, *48*, 5184-5206.

[3] a) X. Y. Fu, Z. Q. Wei, S. Xu, X. Lin, S. Hou, F. X. Xiao, *J. Phys. Chem. Lett.* **2020**, *11*, 9138-9143; b) H. Liang, B. J. Liu, B. Tang, S. C. Zhu, S. Li, X. Z. Ge, J. L. Li, J. R. Zhu, F. X. Xiao, *ACS Catal.* **2022**, *12*, 4216-4226; c) H. Wang, F. Chen, W. Li, T. Tian, *J. Power Sources* **2015**, *287*, 150-157.

[4] a) Y. Z. Bao, X. H. Wu, H. J. Gao, M. M. Zhou, S. Chen, S. Jin, H. Z. Yu, M. Z. Zhu, *Dalton Trans.* **2020**, *49*, 17164-17168; b) Y. Du, Z. J. Guan, Z. R. Wen, Y. M. Lin, Q. M. Wang, *Chem. Eur. J.* **2018**, *24*, 16029-16035; c) A. G. Walsh, P. Zhang, *J. Phys. Chem. Lett.* **2021**, *12*, 257-275; d) X. Q. Ren, X. M. Fu, X. Z. Lin, J. Tang, H. Wang, C. Liu, J. H. Huang, *Eur. J. Inorg. Chem.* **2021**, *2021*, 2281-2283; e) X. Kang, M. Z. Zhu, *Small* **2019**, *15*, e1902703; f) C. Zhu, Z. L. Chen, H. Li, L. Y. Lu, X. Kang, J. Xuan, M. Z. Zhu, *J. Am. Chem. Soc.* **2024**, *146*, 23212-23220; g) M. Kamachi, K. Yonesato, T. Okazaki, D. Yanai, S. Kikkawa, S. Yamazoe, R. Ishikawa, N. Shibata, Y. Ikuhara, K. Yamaguchi, K. Suzuki, *Angew. Chem. Int. Ed.* **2024**, *63*, e202408358; h) X. J. Zou, S. P. He, X. Kang, S. Chen, H. Z. Yu, S. Jin, D. Astruc, M. Z. Zhu, *Chem. Sci.* **2021**, *12*, 3660-3667; i) E. H. Kim, M. H. Lee, J. Kim, E. C. Ra, J. H. Lee, J. S. Lee, *Chin. J. Catal.* **2023**, *47*, 214-221.

[5] a) L. Ji, D. Spanu, N. Denisov, S. Recchia, P. Schmuki, M. Altomare, *Chem. Asian J.* **2020**, *15*, 301-309; b) Z. H. N. Al-Azri, W.-T. Chen, A. Chan, V. Jovic, T. Ina, H. Idriss, G. I. N. Waterhouse, *J. Catal.* **2015**, *329*, 355-367; c) Y. Liu, Y. Li, F. Peng, Y. Lin, S. Yang, S. Zhang, H. Wang, Y. Cao, H. Yu, *Appl. Catal. B Environ.* **2019**, *241*, 236-245.

[6] a) R. Shen, J. Xie, Q. Xiang, X. Chen, J. Jiang, X. Li, *Chin. J. Catal.* **2019**, *40*, 240-288; b) S. M. Thabet, H. N. Abdelhamid, S. A. Ibrahim, H. M. El-Bery, *Sci. Rep.* **2024**, *14*, 10115; c) J. S. Schubert, J. Popovic, G. M. Haselmann, S. P. Nandan, J. Wang, A. Giesriegl, A. S. Cherevan, D. Eder, *J. Mater. Chem. A* **2019**, *7*, 18568-18579; d) P. D. Tran, L. Xi, S. K. Batabyal, L. H. Wong, J. Barber, J. S. Chye Loo, *Phys. Chem. Chem. Phys.* **2012**, *14*, 11596-11599; e) X. Zhao, W. Xie, X. Shao, Z. Wang, B. Yang, C. Yang, J. Wang, X. Su, *Mater. Sci. Semicond. Process.* **2022**, *148*, 106775.

[7] a) M. A. Nazir, T. Najam, M. Altaf, K. Ahmad, I. Hossain, M. A. Assiri, M. S. Javed, A. u. Rehman, S. S. A. Shah, *J. Alloy. Compd.* **2024**, *990*, 174378; b) Z. Fu, X. Ma, B. Xia, X. Hu, J. Fan, E. Liu, *Int. J. Hydrogen Energy* **2021**, *46*, 19373-19384; c) M. Zhai, Z. Li, R. Li, Z. Feng, Q. Wang, C. Zhang, H.

Chi, N. Ta, C. Li, *J. Catal.* **2025**, *443*, 115989; d) J. J. Zhao, P. F. Liu, Y. L. Wang, Y. H. Li, M. Y. Zu, C. W. Wang, X. L. Wang, L. J. Fang, H. D. Zeng, H. G. Yang, *Chem. Eur. J.* **2017**, *23*, 16734-16737; e) J. Zhang, Z. Yu, Z. Gao, H. Ge, S. Zhao, C. Chen, S. Chen, X. Tong, M. Wang, Z. Zheng, Y. Qin, *Angew. Chem. Int. Ed.* **2016**, *56*, 816-820.

View Article Online
DOI: 10.1039/D6SC02262F

[8] J. Shen, C. Luo, S. Qiao, Y. Chen, K. Fu, J. Xu, J. Pei, Y. Tang, X. Zhang, H. Tang, H. Zhang, C. Liu, *Adv. Funct. Mater.* **2023**, *34*, 2309056.

[9] M. Xiao, L. Zhang, B. Luo, M. Lyu, Z. Wang, H. Huang, S. Wang, A. Du, L. Wang, *Angew. Chem. Int. Ed.* **2020**, *59*, 7230-7234.

[10] D. Hikosou, S. Saita, S. Miyata, H. Miyaji, T. Furuike, H. Tamura, H. Kawasaki, *J. Phys. Chem. C* **2018**, *122*, 12494-12501.

[11] X. Liu, N. Fechler, M. Antonietti, *Chem. Soc. Rev.* **2013**, *42*, 8237-8265.

[12] a) J. Ryu, J. H. Seo, G. Song, K. Choi, D. Hong, C. Wang, H. Lee, J. H. Lee, S. Park, *Nat. Commun.* **2019**, *10*, 2351; b) Y. Yuan, W. Xiao, Z. Wang, D. J. Fray, X. Jin, *Angew. Chem. Int. Ed.* **2018**, *57*, 15743-15748.

[13] a) J. P. Holmberg, E. Ahlberg, J. Bergenholtz, M. Hassellöv, Z. Abbas, *J. Colloid Interface Sci.* **2013**, *407*, 168-176; b) A. M. Jastrzębska, P. Kurtycz, A. Olszyna, E. Karwowska, E. Miaśkiewicz‐Pęska, M. Załęska‐Radziwiłł, N. Doskocz, D. Basiak, *Int. J. Appl. Ceram. Technol.* **2014**, *12*, 1157-1173.

[14] a) L. Yang, X. Jiang, W. Ruan, B. Zhao, W. Xu, J. R. Lombardi, *The Journal of Physical Chemistry C* **2008**, *112*, 20095-20098; b) X. Li, Y. Wu, Y. Shen, Y. Sun, Y. Yang, A. Xie, *Appl. Surf. Sci.* **2018**, *427*, 739-744.

[15] Z. Y. Li, Y. H. Chen, J. R. Zhu, Q. Chen, S. J. Lu, F. X. Xiao, *Inorg. Chem.* **2023**, *62*, 16965-16973.

[16] K. Kuroi, M. Yamada, I. Kawamura, M. Jung, C.-G. Pack, F. Fujii, *Phys. Chem. Chem. Phys.* **2022**, *24*, 13356-13364.

[17] A. Li, S. Chen, F. Yang, H. Gao, C. Dong, G. Wang, *Inorg. Chem.* **2021**, *60*, 18337-18346.

[18] a) H. Zhuang, W. Chen, W. Xu, X. Liu, *Int. J. Energy Res.* **2020**, *44*, 3224-3230; b) Y. Yang, X. Li, C. Lu, W. Huang, *Catal. Lett.* **2019**, *149*, 2930-2939.

[19] a) L. Ma, R. Guan, W. Kang, Z. Sun, H. Li, Q. Li, Q. Shen, C. Chen, X. Liu, H. Jia, J. Xue, *J. Colloid Interface Sci.* **2024**, *660*, 381-392; b) X. Shi, L. Mao, C. Dai, P. Yang, J. Zhang, F. Dong, L. Zheng, M. Fujitsuka, H. Zheng, *J. Mater. Chem. A* **2020**, *8*, 13376-13384.

[20] G. Wu, Q. L. Mo, Y. Xiao, K. Wang, X. Z. Ge, S. R. Xu, J. L. Li, Y. Q. Shao, F. X. Xiao, *Inorg. Chem.* **2023**, *62*, 520-529.

View Article Online
DOI: 10.1039/D6SC02262F

[21] Y. Wang, X. H. Liu, Q. Wang, M. Quick, S. A. Kovalenko, Q. Y. Chen, N. Koch, N. Pinna, *Angew. Chem. Int. Ed.* **2020**, *59*, 7748-7754.

[22] K. Wang, X.-Z. Ge, Q.-L. Mo, X. Yan, Y. Xiao, G. Wu, S.-R. Xu, J.-L. Li, Z.-X. Chen, F.-X. Xiao, *J. Catal.* **2022**, *416*, 92-102.

[23] a) G. Malekshoar, A. K. Ray, *Chem. Eng. Sci.* **2016**, *152*, 35-44; b) W. Jones, D. J. Martin, A. Caravaca, A. M. Beale, M. Bowker, T. Maschmeyer, G. Hartley, A. Masters, *Appl. Catal. B Environ.* **2019**, *240*, 373-379.

[24] J.-N. Yuan, X. Yan, B.-X. Zheng, J.-Q. Chen, F.-X. Xiao, *Inorg. Chem. Front.* **2025**, *12*, 1553-1567.

[25] P. Su, S. Li, F. X. Xiao, *Small* **2024**, *20*, 2400958.

[26] L. Wang, Y. Li, Y. Ai, E. Fan, F. Zhang, W. Zhang, G. Shao, P. Zhang, *Adv. Funct. Mater.* **2023**, *33*, 2306466

[27] W. Melitz, J. Shen, A. C. Kummel, S. Lee, *Surf. Sci. Rep.* **2011**, *66*, 1-27.

[28] a) J. Cheng, S. Wan, S. Cao, *Angew. Chem. Int. Ed.* **2023**, *62*, e202310476; b) J. Cheng, W. Wang, J. Zhang, S. Wan, B. Cheng, J. Yu, S. Cao, *Angew. Chem. Int. Ed.* **2024**, *63*, e202406310.

[29] R. Li, H. Li, X. Zhang, B. Liu, B. Wu, B. Zhu, J. Yu, G. Liu, L. Zheng, Q. Zeng, *Adv. Funct. Mater.* **2024**, *34*, 2402797.

[30] a) C. Cheng, B. He, J. Fan, B. Cheng, S. Cao, J. Yu, *Adv. Mater.* **2021**, *33*, 2100317; b) X. Zhang, J. Xu, H. Long, J. Yu, H. Yu, *ACS Catal.* **2024**, *14*, 18669-18678.

[31] a) C. Yang, S. Wan, B. Zhu, J. Yu, S. Cao, *Angew. Chem. Int. Ed.* **2022**, *61*, e202208438; b) Y. Tang, Z.-F. Xu, Y. Sun, C. Wang, Y. Guo, W. Hao, X. Tan, J. Ye, T. Yu, *Energy Environ. Sci.* **2024**, *17*, 7882-7894.

[32] a) W. Zhong, C. Yang, J. Wu, W. Xu, R. Zhao, H. Xiang, K. Shen, Q. Zhang, X. Li, *Chem. Eng. J.* **2022**, *436*, 134813; b) T. Chen, F. Wang, S. Cao, Y. Bai, S. Zheng, W. Li, S. Zhang, S. X. Hu, H. Pang, *Adv. Mater.* **2022**, *34*, 2201779.

[33] M. Liu, Y. Ji, Y. Li, P. An, J. Zhang, J. Yan, S. Liu, *Small* **2021**, *17*, 2102448.

[34] B. He, P. Xiao, S. Wan, J. Zhang, T. Chen, L. Zhang, J. Yu, *Angew. Chem. Int. Ed.* **2023**, *62*, e202313172.

[35] J. Yang, Z. Qiu, C. Zhao, W. Wei, W. Chen, Z. Li, Y. Qu, J. Dong, J. Luo, Z. Li, Y. Wu, *Angew. Chem. Int. Ed.* **2018**, *57*, 14095-14100.

View Article Online
DOI: 10.1039/D6SC02262F

[36] a) J. Deng, X. Xu, B. Su, M. Liu, X. Lin, W. Xing, X. F. Lu, Z. Lan, G. Zhang, S. Wang, *Mater. Horiz.* **2025**, *12*, 5702-5709; b) Z. Wang, B. Su, J. Xu, Y. Hou, Z. Ding, *Int. J. Hydrogen Energy* **2020**, *45*, 4113-4121.

[37] a) S. Sarina, H.-Y. Zhu, Q. Xiao, E. Jaatinen, J. Jia, Y. Huang, Z. Zheng, H. Wu, *Angew. Chem. Int. Ed.* **2014**, *53*, 2935-2940; b) B. Su, K. Tang, J. Cai, X. Lin, W. Xing, K. Liu, X. F. Lu, Y. Hou, W.-J. Ong, S. Wang, *ACS Catal.* **2026**, *16*, 5208-5217.

View Article Online
DOI: 10.1039/D6SC02262F

Data availability statements

The data supporting this article have been included as part of the Supplementary Information.